ISSN 1674-1056
http://cpb.iphy.ac.cn
http://iopscience.iop.org/cpb
中国物理 B
Chinese Physics
中国物理 Chinese Physics B

Narrowband perfect terahertz absorber based on polar-dielectrics metasurface

Meng-Meng Zhao(赵萌萌), Shu-Fang Fu(付淑芳), Sheng Zhou(周胜), Yu-Ling Song(宋玉玲), Qiang Zhang(张强), Yong-Qi Yin(尹永琦), Yu-Tian Zhao(赵玉田), Hong Liang(梁红), Xuan-Zhang Wang(王选章)
Citation: Chin. Phys. B . 2020, 29(5): 054210 . **doi:** 10.1088/1674-1056/ab81fa
Journal homepage: http://cpb.iphy.ac.cn; http://iopscience.iop.org/cpb

What follows is a list of articles you may be interested in

Pancharatnam-Berry metasurface for terahertz wave radar cross section reduction

Shao-He Li(李绍和), Jiu-Sheng Li(李九生)
Chin. Phys. B . 2019, 28(9): 094210 . **doi:** 10.1088/1674-1056/ab33f5

Flexible broadband polarization converter based on metasurface at microwave band

Qi Wang(王奇), Xiangkun Kong(孔祥鲲), Xiangxi Yan(严祥熙), Yan Xu(徐岩), Shaobin Liu(刘少斌), Jinjun Mo(莫锦军), Xiaochun Liu(刘晓春)
Chin. Phys. B . 2019, 28(7): 074205 . **doi:** 10.1088/1674-1056/28/7/074205

Aperture efficiency and mode constituent analysis for OAM vortex beam generated by digital metasurface

Di Zhang(张迪), Xiangyu Cao(曹祥玉), Huanhuan Yang(杨欢欢), Jun Gao(高军), Shiqi Lv(吕世奇)
Chin. Phys. B . 2019, 28(3): 034204 . **doi:** 10.1088/1674-1056/28/3/034204

Wideband linear-to-circular polarization conversion realized by a transmissive anisotropic metasurface

Bao-Qin Lin(林宝勤), Jian-Xin Guo(郭建新), Bai-Gang Huang(黄百钢), Lin-Bo Fang(方林波), Peng Chu(储鹏), Xiang-Wen Liu(刘湘雯)
Chin. Phys. B . 2018, 27(5): 054204 . **doi:** 10.1088/1674-1056/27/5/054204

Double-rod metasurface for mid-infrared polarization conversion

Yang Pu(蒲洋), Yi Luo(罗意), Lu Liu(刘路), De He(何德), Hongyan Xu(徐洪艳), Hongwei Jing(景洪伟), Yadong Jiang(蒋亚东), Zhijun Liu(刘志军)
Chin. Phys. B . 2018, 27(2): 024202 . **doi:** 10.1088/1674-1056/27/2/024202

Narrowband perfect terahertz absorber based on polar-dielectrics metasurface*

Meng-Meng Zhao(赵萌萌)[1], Shu-Fang Fu(付淑芳)[1,†], Sheng Zhou(周胜)[1,2,‡], Yu-Ling Song(宋玉玲)[1], Qiang Zhang(张强)[1], Yong-Qi Yin(尹永琦)[1], Yu-Tian Zhao(赵玉田)[1], Hong Liang(梁红)[3], and Xuan-Zhang Wang(王选章)[1]

[1] *Key Laboratory for Photonic and Electronic Bandgap Materials (Ministry of Education), School of Physics and Electronic Engineering, Harbin Normal University, Harbin* 150025, *China*

[2] *Department of Electrical Engineering, University of California, Riverside, California* 92521, *USA*

[3] *School of Technology, Harbin Normal University, Harbin* 150086, *China*

(Received 12 December 2019; revised manuscript received 5 February 2020; accepted manuscript online 23 March 2020)

We theoretically propose a narrowband perfect absorber metasurface (PAMS) based on surface phonon polaritons in the terahertz range. The PAMS has unit cell consisting of a silver biarc on the top, a thin polar-dielectric in the middle and a silver layer at the bottom. The phonon polaritons are excited at the interface between the silver biarc and the polar dielectric, and enhance the absorption of the PAMS. The absorption peak is at 36.813 μm and the full width half maximum (FWHM) is nearly 36 nm, independent of the polarization and incidence angle. The electric fields are located at the split of the biarc silver layer and the quality factor Q is 1150. The FWHM decreases with the decreasing split width. When the thickness of the bottom layer is larger than 50 nm, the narrow band and high absorption are insensitive to the thickness of those layers. The designed absorber may have useful applications in terahertz spectra such as energy harvesting, thermal emitter, and sensing.

Keywords: metasurface, narrowband perfect absorber, terahertz, polar-dielectrics

PACS: 78.30.–j, 78.20.–e, 42.25.Ja, 42.25.Bs **DOI:** 10.1088/1674-1056/ab81fa

1. Introduction

Metasurfaces (MSs) are artificial dielectric metamaterials, which are composed of metal elements with subwavelength size in periodic or nonperiodic arrangement.[1,2] MSs support integration and miniaturization of optical components and control the amplitude, phase, and polarization of the reflected wave. Many interesting physical effects were realized, such as super resolution imaging,[3] optical cloaking,[4] and negative refraction.[5]

Perfect absorber metasurfaces (PAMSs) have attracted tremendous interest recently. They exhibit nearly total absorption in a special frequency range. In general, a PAMS is structured as follows: a metallic resonators layer, a subwavelength-thick dielectric layer and a highly reflective layer.[6] A perfect absorber (PA) has a unity absorption band in gigahertz,[7] terahertz,[8] visible light,[9] or infrared bands.[10] Many narrowband metasurface absorbers have been proposed, including steering,[11] focusing,[12] total absorption,[13] solar photovoltaic cells,[14] heat radiations,[15] photo-detections,[16] and so on.[17,18] Deng *et al.*[19] proposed a facile metagrating hologram approach to address the fundamental limits of both bandwidth and angle tolerance experienced by phasegradient metasurfaces. The dual-way polarization-switchable vectorial meta-holograms realized by our proposed diatomic metasurfaces provide a new paradigm for a variety of polarization-encrypted anophotonic applications with drastically enhanced capacity and security.[20] Li *et al.*[21] reported a two-dimensional structure with periodically arranging a large number of individual absorber units in the horizontal and vertical directions. The reflection loss from 9.2 GHz to 18.0 GHz is under −10 dB (the bandwidth reaches 8.8 GHz), and the peak of S_{11} is −14.4 dB.

Some of representative results of different kinds of narrowband metasurface absorbers are given in Table 1. Various metasurfaces have their own distinctive characteristics, opening new opportunities for electromagnetic wave manipulation. The absorption frequency region covering from microwaves to ultraviolet. Various kinds of localized optical resonances are commonly used to realize narrowband absorption (e.g., Mie resonances,[22] plasmonicresonances,[23] surface plasmon resonances,[24] lattice resonance[34]). For the narrowband absorbers, the higher the Q-factor or the figure-of-merit (FOM) is, the better the sensitivity is. Thus, a structure with high Q-factor or FOM has a potential application as a sensor.

*Project supported by the National Natural Science Foundation of China (Grant No. 11204056), Harbin Normal University Master's Innovation Project (Grant Nos. HSDSSCX2018-77 and HSDSSCX2018-79), Key Laboratory of Engineering Dielectrics and Its Application (Harbin University of Science and Technology), Ministry of Education, China (Grant No. KF20171110), and Natural Science Foundation of Heilongjiang Province, China (Grant No. LH2019A028).

†Corresponding author. E-mail: shufangfu1975@163.com

‡Corresponding author. E-mail: zhousheng_wl@126.com

© 2020 Chinese Physical Society and IOP Publishing Ltd

Table 1. Frequency range, wavelength, frequency, absorption efficiency, quality factor and figure-of-merit of narrowband metasurface absorbers.

Frequency range	Wavelength	Frequency	Absorption efficiency	Quality factor	FOM	References
Microwave	1.5, 3 mm	$10, 20 \times 10^9$	Near 100%	54.3, 66.7		2018[22]
THz	167.48 μm	1.79×10^{12}	99.4%	474	38.8/RIU	2019[23]
	116.20 μm	2.58×10^{12}	98.86%	385.07		2017[24]
Mid-infrared	12.9 μm	2.3240×10^{13}	80%	170		2019[25]
	1.6085 μm	1.86×10^{14}	100%		36.4	2017[26]
	2.6055 μm	1.15×10^{14}			3.14	
Near infrared	2403.15nm	1.2475×10^{14}	>98%		3640	2017[27]
	1.550 μm	1.9341×10^{14}	>99%	221.43	214.29	2018[28]
	1.55 μm	1.9341×10^{14}	99.8%		1329	2018[29]
	1500–1850 nm	$1.62–1.99 \times 10^{14}$	100%		2.91	2019[30]
	1.47 μm	2.0394×10^{14}	100%		6400	2018[31]
	1150 nm	2.6069×10^{14}	100%		374	2018[32]
	1125 nm	2.6648×10^{14}	100%		338.6	2018[33]
	930 nm	3.2236×10^{14}	99%		63	2017[34]
Visible light	750 nm	3.9972×10^{14}	95%		233.5	2017[35]
	700–800 nm	$3.74–4.28 \times 10^{14}$	99.67%	14.78		2019[36]
	642 nm	4.6697×10^{14}				2019[37]
	824 nm	3.6383×10^{14}	99.95%		50.3	
	711 nm	4.2165×10^{14}	100%	356		2019[38]
	503.5 nm	5.9542×10^{14}	99.969%		92333/RIU	2019[39]
Ultraviole	176.1 nm	1.7024×10^{15}	85%		483	2018[40]

A phonon polariton means that optical-phonon modes of lattice vibration couple with electromagnetic waves.[37] Polaritons in polar-dielectrics provide possibly strong photon confinement. The phonon polaritons are less lossy due to the charge neutral and bosonic nature of the phonons. The phonon polaritons have longer propagation lengths and lifetimes. Specifically, surface phonon polaritons (SPhPs) supported on polar crystals,[38] such as SiC,[39] h-BN[40] and TlBr,[41] have inherent long lifetimes (∼1 ps) and low optical loss,[31] but surface plasmon polaritons (SPPs) in metals, which are lossy with a lifetime of ∼10 fs.[42] Confinement factors ($\beta = \lambda_0/\lambda_p$, defined as the ratio of free space photon propagation wavelength to polariton wavelength) of over 40 have been achieved for both h-BN phonon polaritons,[43] which means that infrared wave (5–20 μm) can be modulated with wavelength down to a few hundreds of nanometers. This ability to localize light to achieve deep subwavelength control is of great technological significance as it allows the integration of the merits of both electronics and photonics at high device density into a single technology.[44] At room temperature, TlBr is stable in the CsCl structure. Thallium bromide shows great promise for room temperature gamma ray spectroscopy due to its well-suited material properties and the relative ease with which it can be grown in bulk.[45]

In this paper, we propose a narrowband PAMS based on a polar-dielectrics crystal. The PAMS is a sandwiched structure composed of a biarc silver structure and a silver layer separated by a thin TlBr layer. All the simulations are performed in the COMSOL Multiphysics software with an RF module. Some basic points for the model and simulation are as follows: the perfect matched layer (PML) boundary conditions were used on the top and bottom surfaces. A symmetric periodic boundary condition was used along the x and y directions. It is noted that periodicity is a basic requirement for metasurfaces, and thus periodic boundary conditions are applied in the simulations. The reflection and transmission spectra were computed via the "S parameter" analysis object, which makes use of a plane-wave excitation source incident from upside to the PAMS.

2. Structure design and simulation

The PAMS consists of three functional layers, as shown in Fig. 1(a). The top layer consists of a biarc silver structure with thickness d_{ms}, which is responsible for the electromagnetic response. The middle polar-dielectrics crystal (PC) layer with a thickness d_p offers the required multi-reflection resonance path necessary for destructive interference. The bottom Ag layer with thickness d_m is used to completely eliminate the transmission of an electromagnetic wave through the Ms. I and R are the incident and reflected waves, respectively, while θ represents the angle between the incidence and z-axis. The incidence wave and z-axis plane constitute the incidence plane, while β represents the angle between the incidence plane and the x-axis. The upper space and the bottom space are air.

For subsequent theoretical and numerical calculations, the permittivity of polar dielectrics is $\varepsilon_{pc} = \varepsilon_h + (\varepsilon_l - \varepsilon_h)\omega_T^2/(\omega_T^2 - \omega^2 - i\omega^2\tau)$, wherein ω_T is the frequency of the transverse optical phonon and τ is the damping responsible for losses. We assume that PC is a TlBr crystal with $\omega_T = 48.0\ \mathrm{cm}^{-1}$, $\varepsilon_h = 5.34$, $\varepsilon_l = 30.4$ and $\tau = 0.01$.[36] The permittivity of silver layers is defined as $\varepsilon_m = \varepsilon_\infty - (\varepsilon_o -$

$\varepsilon_\infty)\omega_p^2/(\omega^2 - i\omega^2\tau')$, which appears to be appropriate for the top surface and bottom layer. The physical parameters of Ag are taken as $\omega_p = 1.419 \times 10^{16}$ rad/s, $\varepsilon_\infty = 4.017$, $\varepsilon_o = 4.896$ and $\tau' = 0.01$.[37] A unit cell of the biarc silver layer is also shown in Fig. 1(b). The geometry dimensional parameters of the unit cell are as follows: We fixed the length of the square $a = 6$ μm, the outer radius $r_1 = 2.5$ μm, the inner radius $r_2 = 2.2$ μm, the width of the strip $d_1 = 0.3$ μm and the width of a split $d_2 = 0.3$ μm with the angle α, the thickness $d_{pc} = 2$ μm, $d_m = 100$ nm and $d_{ms} = 100$ nm. The reflection and transmission are given by $R = |r/I|^2$ and $T = |t/I|^2$. The absorption coefficient (AC) A is calculated by applying the following equation $A = 1 - R - T$.

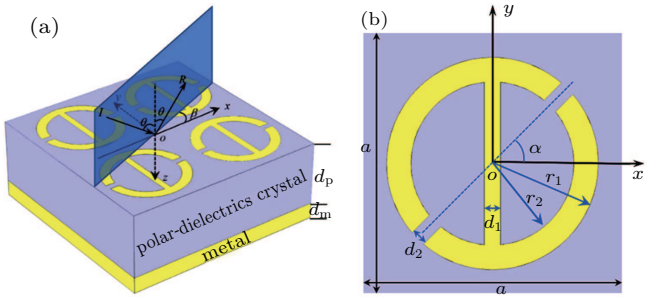


Fig. 1. (a) Conceptual illustration of the proposed three-layered metasurface consisting of the TiBr layer sandwiched by top biarc silver surface and a bottom silver layer. (b) The top view of circularly-polarized metallic sub-cell.

3. Results and discussions

The absorption of PAMS with TE wave normal incidence are shown in Fig. 2. In order to show the influence of the phonon polaritons, we have simulated the absorption of PC layer and PAMs. For fixed PC thickness, the absorption of PAMS of TE wave (black line) and TM wave (blue line) is significantly larger than that of PC layer (red line). For TE wave, the maximum absorption is 99.99% at center of 36.816 μm with absorption FWHM of 32 nm. To analyze the localization of the PAMS, we calculate the quality factor $Q = \lambda/\Delta\lambda = 1150$, where $\Delta\lambda$ is the FWHM of the absorption. For TM wave, the maximum absorption is only 76.7%. The inset of Fig. 2 shows the electric field patterns (arrows for the direction and color for the intensity) at interface of biarc silver and polar-dielectrics crystal at the absorption peaks. For TE wave normal incidence, the electric fields are parallel to the PAMS surface and along the y-axis, the electric field focuses on both sides of the split in biarc structure. The maximum of the induced electric field is larger than that of the incident wave nearly 20 times. For TM polarization, the magnetic field is along the y-axis and the electric field is along the x-axis, the induced electric field is larger than that of the incident wave only 2.5 times. The electric field is highly localized for TE wave incidence, resulting in absorption of TE larger than TM polarization. The absorption peak is located at center of 36.816 μm, i.e., 8.143 THz for TM polarization. The narrow-band perfect absorber will provide the great potential applications to filters and plasmonic refractive index sensors.

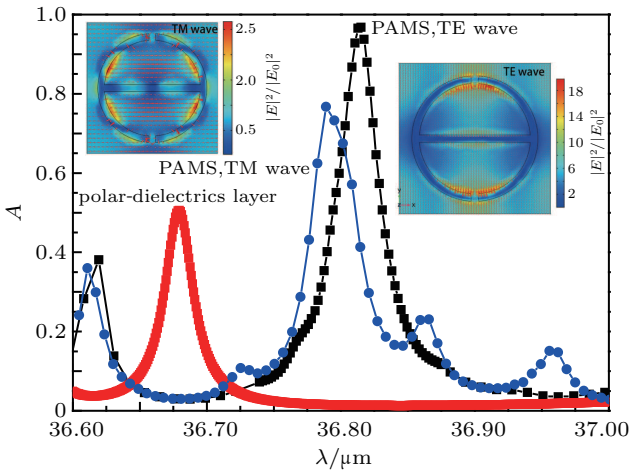


Fig. 2. Absorption spectra of TE and TM wave incidence. The red line for the PC layer with TE wave, black line for PAMS with TE wave and blue line for PAMS with TE wave. The inset shows the electric field patterns at the absorption peak of the PAMS for TE and TM polarizations.

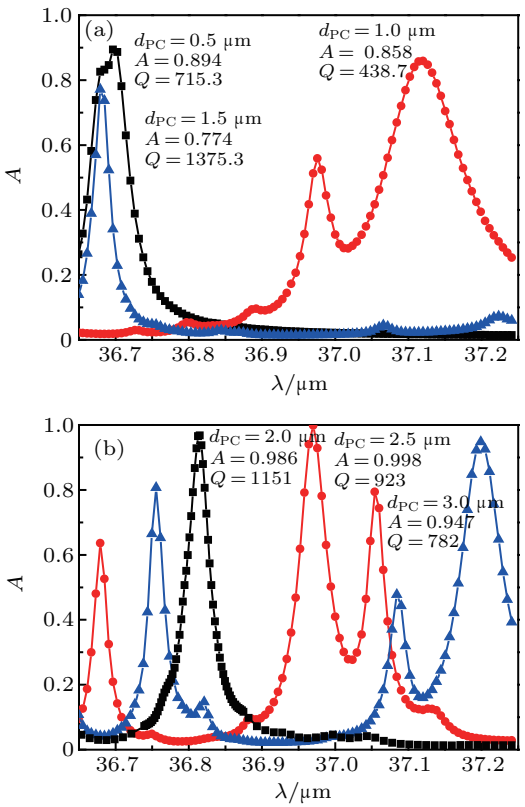


Fig. 3. Absorption spectra of the PAMS with the PC layer thickness from 0.5 μm to 3.0 μm for TE wave incidence: (a) the PC layer thickness from 0.5 μm to 1.5 μm, (b) the PC layer thickness from 2.0 μm to 3.0 μm.

To investigate the effect of the PC layer thickness values on the absorption amplitudes, we sweep the thicknesses from 0.5 μm to 3.0 μm with a step size of 0.5 μm. The effect of layer thicknesses on the absorption amplitudes is shown in Fig. 3. The PC layers with various thicknesses produced different absorption amplitudes ranging from 0.774 to

0.998. For $d_{PC} = 2.0$ μm and 2.5 μm, the PAMS is a perfect absorber. It is worth mentioning that absorption spectra of $d_{PC} = 2.0$ μm have one absorption peak with high Q. For the following analyses, we choose the thickness of the PC layer to be $d_{PC} = 2.0$ μm.

An important characteristic feature of the PAMS is the angular independence of the incident wave. This is very useful in thermal imaging/sensing and energy harvesting applications to receive off incident wave. Figure 4 shows the angular dispersions of the absorbance peak at various angles (θ) of incidence for both TE and TM configurations. For the TE polarization (Fig. 4(a)), the perfect absorption at the wavelength of 36.8163 μm with FWHM of 32 nm was maintained up to 60°. The wavelength of absorption peak is not shifted as the incident angle increases from 0° to 80°, the magnetic field cannot drive the localize efficiently at large angles. For larger angle incidence, the maximum of the induced electric field is larger than that of the incident wave only 1.6 times, as seen in Fig. 4(c). However, in normal incidence, the maximum of the induced electric field is larger than that of the incident wave only 20 times, as seen in Fig. 2. The electric field is about an order of magnitude lower than that in normal incidence, so the absorption efficiency is obviously reduced. Conversely, for the TM polarization (Fig. 4(b)), the absorbance peak is nearly independent of the incident angle. This is because the direction of the magnetic field of the incident light remains unchanged with various incident angles and it can efficiently localize at all angles of incidence, so the PA has good angular independence. For larger angle incidence, the electric field remains larger than that of the incident wave 3–4 times, so the absorption is also stable, as seen in Fig. 4(d).

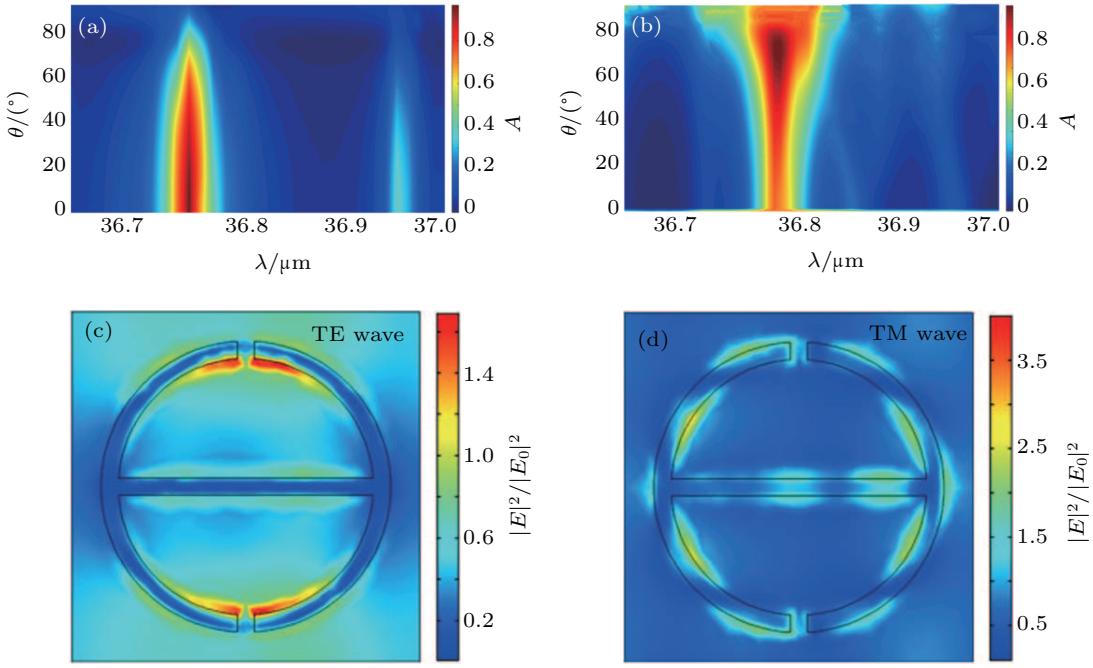


Fig. 4. Color plot of angular dependence (θ) of absorption: (a) TE polarization, (b) TM polarization. The electric field patterns at the top surface of PA with (c) TE and (d) TM waves for $\theta = 80°$.

Next, we investigate the polarization-angle dependence of the PA. We employed a TE wave with switching the incident plane angle (β) to illuminate the structure, the absorption is maintained normal incident, as shown in Fig. 5. For normal incidence, TE and TM indicate $\beta = 0°$ and $\beta = 90°$, respectively. The wavelengths of the absorption peak for TE and TM waves are 36.8163 μm and 36.7889 μm, respectively. For the incidence wave from TE wave to TM wave, the absorption of the PA is blue-shifted as β increases, $\Delta_\lambda = (\lambda_{TM} - \lambda_{TE})/\lambda_{TE} \sim 0.07\%$. Figures 5(b) and 5(c) show the electric field patterns for $\beta = 45°$ and 90° (arrows for the direction and color for the intensity) at the top of PA at their absorption peaks. For $\beta = 0°$ that is TE wave, the electric field pattern is shown in Fig. 2(b). For $\beta = 45°$, the electric field focuses on four areas at the boundary of Ag and PC, the maximum of the electric field is larger than that of incident wave nearly 15 times, as shown in Fig. 4(b). For $\beta = 90°$ of TM wave, the electric field is along the x-axis, the electric field enhancement is located at eight areas around the biarc, as shown in Fig. 5(c). The electric field inside the biarc is larger than that outside the biarc. For TM wave, the maximum of the electric field is smaller than that of TE wave.

To discuss the tolerance of fabricating the PAMS, we simulate the effect of the split width d_2 and the angle α. For a fixed split width, the angle of the split has little effect on wavelength and FWHM of the absorption peak, as shown in Fig. 6. We have chosen five angles to simulation, the deviation of the wavelength of absorption peaks are smaller than 10 nm

and the absorptivity has ranged from 97% ($\alpha = 0°$) to 91% ($\alpha = 60°$). The electric field patterns of those angles are shown in Fig. 6(b). The maximum of the electric field is larger than that of the incident wave nearly 18 times, the electric fields are located near the split.

For a fixed split angle, the split width has little effect on the wavelength of the absorption peak and enhances the FWHM of the PAMS, as shown in Fig. 7. For the split width from 0.5 μm to 2.0 μm, the FWHMs increase from 36.9 nm to 40 nm. The results show that the FWHMs decrease with the decreasing split width. The maximum of the electric fields decreases from 18 times to 14 times of the incident wave.

We set the biarc structure and bottom layers as silver and took the thicknesses 5 nm, 10 nm, 50 nm and 150 nm at an TE wave normal incidence. The thickness of the biarc structure has little effect on absorption shown in Fig. 8(a). However, the bottom layer has effect on absorption. The corresponding absorption ranges from 0.65 to 0.98 as seen in Fig. 8(b). It can be observed that the absorption peaks are insensitive to variation of thickness of silver larger than 50 nm. In the studied

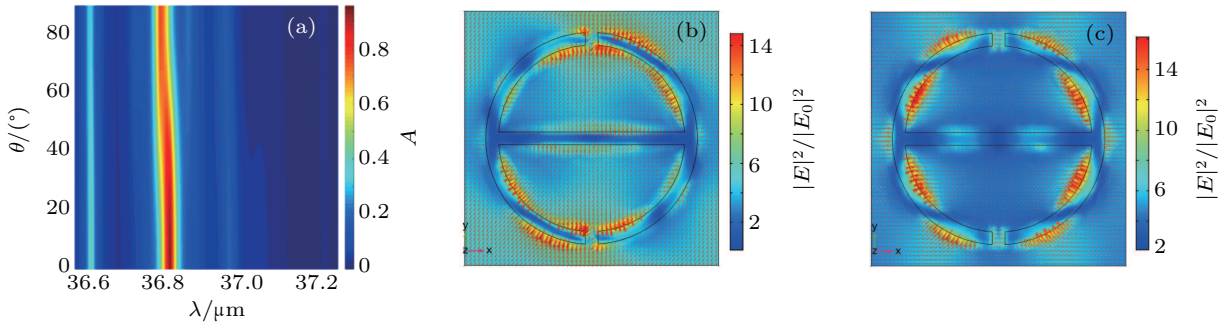


Fig. 5. Color plot of angular dependence (β) of absorption: (a) absorption of PA, and the electric field patterns at the top surface of PA with (b) $\beta = 45°$ and (c) $\beta = 90°$.

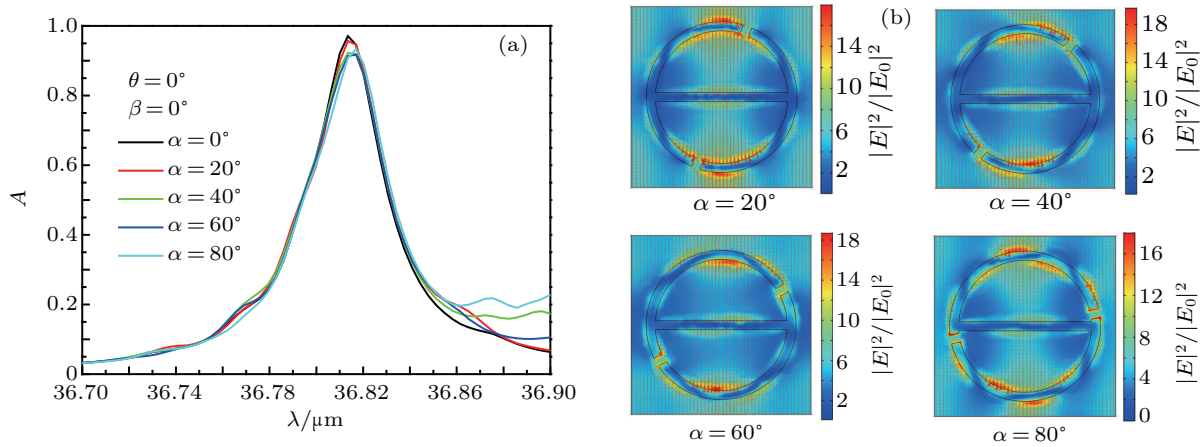


Fig. 6. Absorption spectra for angular dependence (α): (a) absorption of PA, and (b) the electric field patterns at the top surface of PA with $\alpha = 20°, 40°, 60°$ and $80°$.

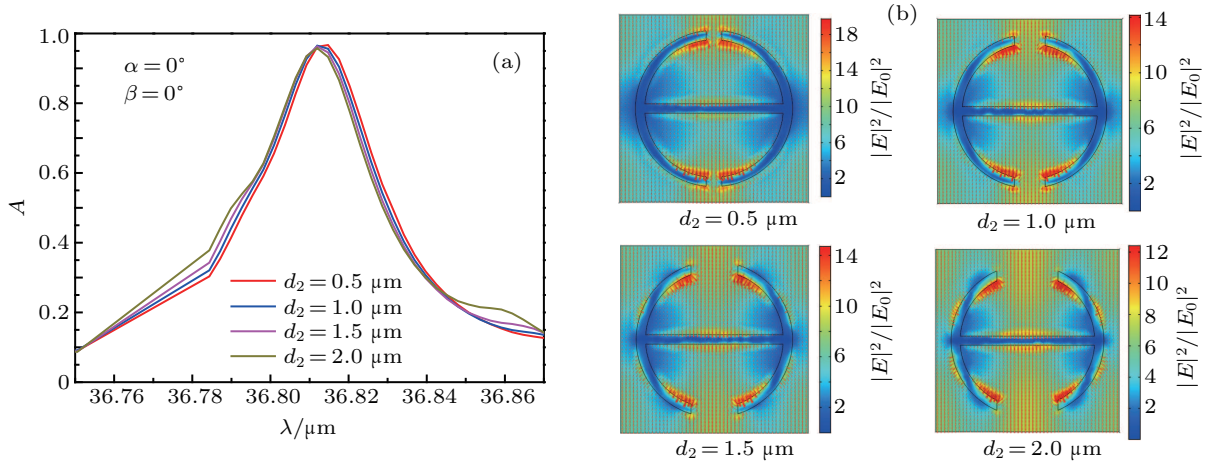


Fig. 7. Absorption spectra for the split width: (a) absorption of PA, and (b) the electric field patterns at the top surface of PA with $d_2 = 0.5$ μm, 1.0 μm, 1.5 μm, and 2.0 μm.

regimes, the peak absorbance remains higher than 98% and the resonant wavelength is also stable. Thus, we choose the thicknesses of the biarc structure and the bottom layer to be 100 nm to eliminate the transmission wave. All these features are of importance to practical fabrication and applications.

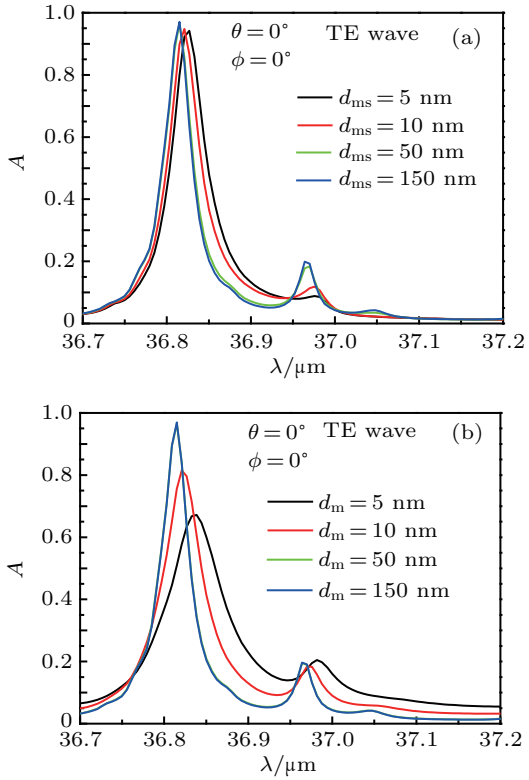


Fig. 8. Absorption spectra for the biarc structure and bottom layer thickness: (a) the biarc structure thickness, and (b) bottom layer thicknesses d_{ms} = 5 nm, 10 nm, 50 nm and 150 nm.

4. Conclusion

We have numerically investigate design of a narrowband PAMS. The absorber is composed of a biarc silver structure layer, a TlBr layer, and a silver ground layer. Several possibilities in the geometry of the structure are taken into consideration to obtain the PAMS. Such a PAMS is analyzed by scaling various design parameters. The simulation results show that the PAMS is obtained with the absorption at 36.813 μm and the FWHM nearly 36 nm. The absorption is insensitive to the polarization and strip angle, and the FWHM decreases with the decreasing split width. When the thicknesses of the biarc structure and the bottom layer are larger than 50 nm, the narrow band and high absorption are insensitive to the thickness of those layers. This study can be used for THz imaging and detection design.

References

[1] Ding F, Yang Y Q, Deshpande R A and Bozhevolnyi S 2018 *Nanophotonics* **7** 1129
[2] Liu Y H and Zhao X P 2018 *Chin. Phys. B* **27** 117805
[3] Gao H, Pu M B, Li X *et al.* 2017 *Opt. Express.* **25** 13933
[4] Yang J N, Huang C, Wu X Y, Sun B and Luo X G 2018 *Adv. Opt. Mater* **6** 1800073
[5] Liu B Y, Ren B, Zhao J J *et al.* 2018 *Sci. Rep.* **8** 15210
[6] Liu G D, Zhai X, Meng H Y *et al.* 2018 *Opt. Express* **26** 11471
[7] Chen W J, Chen R, Zhou Y and Ma Y G 2019 *Opt. Lett.* **44** 1076
[8] Ashoori V and Shayganmanesh M 2019 *Appl. Phys. B* **125** 40
[9] Akhavan A , Abdolhosseini S, Ghafoorifard H and Habibiyan H 2018 *J. Lightwave. Technol.* **36** 5593
[10] Zhao D W, Yu Y, Wang C L *et al.* 2017 *Nat. Energy.* **2** 17018
[11] Matsuno Y and Sakurai A 2017 *Opt. Commun.* **385** 118
[12] Ghobadi A, Hajian H, Butun B and Ozbay E 2018 *ACS Photon.* **5** 4203
[13] Pawliszewska M, Duzynska A, Zdrojek M and Sotor J 2019 *Opt. Express* **27** 11361
[14] Li Y Y, Liu Z Q and Zhang H J 2019 *Opt. Express* **27** 11809
[15] Liao Y L and Zhao Y 2015 *Plasmonics* **10** 1219
[16] Kang S, Qian Z Y, Rajaram V *et al.* 2019 *Adv. Opt. Mater.* **7** 1801236
[17] Luo X, Liu Z M, Wang L L *et al.* 2018 *Appl. Phys. Express* **11** 105102
[18] Liu N, Mesch M, Weiss T, Hentschel M and Giessen H 2010 *Nano Lett.* **10** 2342
[19] Deng Z L, Deng J H, Zhuang X *et al.* 2018 *Light-Sci. Appl.* **7** 78
[20] Deng Z L, Deng J H, Zhuang X *et al.* 2018 *Nano Lett.* **18** 2885
[21] Li Y H, Deng L W, Luo H *et al.* 2019 *Acta Phys. Sin.* **68** 095201 (in Chinese)
[22] Su X F, Li G H, Yang H *et al.* 2018 *Plasmonics* **13** 729
[23] Geng Z, Su W, Wang X Y, Jiang Y F and Liu Y 2019 *Optik* **194** 163071
[24] Wang B X, Huang W Q and Wang L L 2017 *RSC Adv.* **7** 42956
[25] Howes A, Nolen J R, Caldwell J D and Valentine J 2020 *Adv. Opt. Mater.* **8** 1901470
[26] Aslan E, Kaya S, Aslan E *et al.* 2017 *Sens. Actuat. B-Chem.* **243** 617
[27] Li R F, Wu D, Liu Y M *et al.* 2017 *Nanoscale Res. Lett.* **12** 1
[28] Wu D, Yang L, Liu C *et al.* 2018 *Nanoscale Res. Lett.* **13** 144
[29] Zhao Z Y, Li G H, Yu F L *et al.* 2018 *Plasmonics* **13** 2267
[30] Madadi Z, Abedi K, Darvish G and Khatir M 2019 *Optik* **183** 670
[31] Chen C, Wang G, Zhang Z Y and Zhang K 2018 *Opt. Lett.* **43** 3630
[32] Wang L, Sang T, Li J L *et al.* 2018 *J. Mod. Opt.* **65** 1601
[33] Zhao L, Liu H, He Z H and Dong S K 2018 *Opt. Commun.* **420** 95
[34] Zhang M, Fang J W, Zhang F *et al.* 2017 *Opt. Commun.* **405** 216
[35] Wu D, Li R F, Liu Y M *et al.* 2017 *Nanoscale Res. Lett.* **12** 427
[36] Chau Y F C, Chao C T C, Huang H J *et al.* 2019 *Results Phys.* **15** 102567
[37] Li Y Y, Liu Y, Liu Z Q *et al.* 2019 *Appl. Phys. Express* **12** 072002
[38] Meng L J, Zhao D, Yang Y Q *et al.* 2019 *Phys. Rev. Appl.* **11** 044030
[39] He K, Liu Y D and Fu Y Q 2019 *Nanomaterials* **9** 603
[40] Wang L, Sang T, Gao J, Yin X and Qi H L 2018 *Appl. Opt.* **57** 7338
[41] Ray A, Smith H M and Haegel N M 2014 *J. Appl. Phys.* **115** 163709
[42] Caldwell J D, Lindsay L, Giannini V *et al.* 2015 *Nanophotonics* **4** 44
[43] Khurgin J B 2015 *Nat. Nanotechnol.* **10** 2
[44] Zhang Q, Zhen Z, Liu C P *et al.* 2019 *Opt. Express* **27** 18628
[45] Smith H M, Zhou Y Z, Ciampi G *et al.* 2013 *Appl. Phys. Lett.* **103** 091901
[46] Hinson D C and Stevenson J R 1967 *Phys. Rev.* **159** 711
[47] Mitra S S and Massa N E 1982 *Lattice Vibrations in Semiconductors* in *Handbook on Semiconductors* ed Paul W (Amsterdam: North-Holland Publishing Company) Vol. 1 Chap. 3
[48] Johnson P B and Christy R W 1972 *Phys. Rev. B* **6** 4370